

# Resonant Sterile Neutrino Dark Matter in the Local and High- $z$ Universe

Brandon Bozek<sup>1\*</sup>, Michael Boylan-Kolchin<sup>1</sup>, Shunsaku Horiuchi<sup>2</sup>,  
Shea Garrison-Kimmel<sup>3</sup>, Kevork Abazajian<sup>4</sup>, and James S. Bullock<sup>4</sup>

<sup>1</sup>*Department of Astronomy, The University of Texas at Austin, 2515 Speedway, Stop C1400, Austin, TX 78712, USA*

<sup>2</sup>*Center for Neutrino Physics, Department of Physics, Virginia Tech, Blacksburg, VA 24061, USA*

<sup>3</sup>*TAPIR, California Institute of Technology, Pasadena, CA 91125, USA*

<sup>4</sup>*Department of Physics and Astronomy, University of California at Irvine, Irvine, CA 92697, USA*

16 December 2015

## ABSTRACT

Sterile neutrinos comprise an entire class of dark matter models that, depending on their production mechanism, can be hot, warm, or cold dark matter. We simulate the Local Group and representative volumes of the Universe in a variety of sterile neutrino models, all of which are consistent with the possible existence of a radiative decay line at  $\sim 3.5$  keV. We compare models of production via resonances in the presence of a lepton asymmetry (suggested by Shi & Fuller 1999) to “thermal” models. We find that properties in the highly nonlinear regime – e.g., counts of satellites and internal properties of halos and subhalos – are insensitive to the precise fall-off in power with wavenumber, indicating that nonlinear evolution essentially washes away differences in the initial (linear) matter power spectrum. In the quasi-linear regime at higher redshifts, however, quantitative differences in the 3D matter power spectra remain, raising the possibility that such models can be tested with future observations of the Lyman- $\alpha$  forest. While many of the sterile neutrino models largely eliminate multiple small-scale issues within the Cold Dark Matter (CDM) paradigm, we show that these models may be ruled out in the near future via discoveries of additional dwarf satellites in the Local Group.

**Key words:** Galaxy: halo – Local Group – cosmology: theory – large-scale structure of Universe – dark matter

## 1 INTRODUCTION

The triumphs of the now-standard  $\Lambda$ CDM model are manifold (see [Frenk & White 2012](#) and [Primack 2015](#) for recent reviews). Nagging doubts about  $\Lambda$ CDM on small scales (corresponding to linear perturbations with masses of  $\lesssim 10^{10} M_{\odot}$ ) have lingered, however, owing in large part to the difficulty of modeling low-mass perturbations from the linear to the nonlinear regime. In studying the highly nonlinear regime, a number of issues have arisen on these scales. In particular, several possible conflicts exist between theory and observations on the scale of dwarf galaxies ( $M_{\star} \lesssim 0.1 L^{\star}$  or  $M_{\text{halo}} \lesssim 10^{11} M_{\odot}$  at  $z = 0$ ). These small-scale issues include: the over-prediction of the abundance of low-mass dark matter halos relative to the observed number of satellite galaxies in the Local Group (the Missing Satellites Problem – [Klypin et al. 1999](#); [Moore et al. 1999](#)), the prediction of a central cusp in the dark matter halo density profile while the

density profile of dwarf galaxies inferred from observations favor a core (the Core-Cusp Problem – [Flores & Primack 1994](#); [Moore 1994](#)), and the over-prediction of the density in the subhalos expected to host the bright, classical Milky Way dwarf galaxies (the Too Big To Fail (TBTf) Problem – [Boylan-Kolchin et al. 2011, 2012](#)).

Within the CDM paradigm, the resolution to these issues must lie in the baryonic physics of galaxy formation. A combination of (global) photoionization and stellar feedback may suppress star formation below some mass threshold, which would resolve the Missing Satellites Problem ([Bullock et al. 2000](#); [Kravtsov et al. 2004](#)). Proposed resolutions of the Core-Cusp problem and the TBTf issue require supernova-driven gravitational potential fluctuations that remove substantial quantities of dark matter from the center of dark matter halos (possibly in concert with tidal stripping) to flatten cuspy density profiles into cores ([Governato et al. 2010](#); [Brook et al. 2011](#); [Governato et al. 2012](#); [Zolotov et al. 2012](#); [Di Cintio et al. 2014](#); [Oñorbe et al. 2015](#)). There is some debate in the literature as to whether these solutions

\* bozek@astro.as.utexas.edu

**Table 1.** WDM Models. *Column 1:* Model label; *Column 2:* Physical parameter that defines the model: cosmological lepton number ( $L$ ), mixing angle between sterile and active neutrinos ( $\sin^2(2\theta)$ ), or thermal WDM particle mass ( $m$ ); *Column 3:* Half-mode mass; *Column 4:* Was a Local Group pair simulated for this model?; *Column 5:* Final redshift of the cosmological volume simulation.

Model	Physical Parameter	$M_{1/2} [h^{-1} M_\odot]$	Local Group pair	$z_f$
L46	$L = 4.6 \times 10^{-4}$	$2.1 \times 10^8$	yes	2
THM2.9	$m = 2.9 \text{ keV}$	$2.4 \times 10^8$	no	2
S220	$\sin^2(2\theta) = 20 \times 10^{-11}$	$2.2 \times 10^8$	no	2
L7	$L = 7 \times 10^{-4}$	$7.8 \times 10^8$	yes	0
THM2	$m = 2 \text{ keV}$	$9.4 \times 10^8$	yes	0
S229	$\sin^2(2\theta) = 2.9 \times 10^{-11}$	$8.2 \times 10^8$	yes	0
L8	$L = 8 \times 10^{-4}$	$2.1 \times 10^9$	yes	2
THM1.6	$m = 1.6 \text{ keV}$	$1.8 \times 10^9$	no	2
S208	$\sin^2(2\theta) = 0.8 \times 10^{-11}$	$1.9 \times 10^9$	no	2

can be generally viable (Peñarrubia et al. 2012; Garrison-Kimmel et al. 2013). In particular, the TBTF problem is also an issue for Local Group and field halos, where stripping is unlikely to occur (Garrison-Kimmel et al. 2014b; Kirby et al. 2014; Papastergis et al. 2015). The CDM small-scale issues extending beyond the virial radii of the Milky Way (MW) and Andromeda (M31) galaxies underscore the importance of studying the Local Group as a whole.

These small-scale issues in CDM have led to a re-consideration of Warm Dark Matter (WDM) models of structure formation. In WDM scenarios, dark matter has a cosmologically-important free-streaming scale that erases primordial perturbations below a characteristic scale, one that is relevant for galaxy formation. For example, a  $\sim 2$  keV Dark Matter (DM) particle produced in thermal equilibrium reduces power for (linear) wavenumbers larger than  $k \sim 10 h \text{ Mpc}^{-1}$ , corresponding to (linear) mass scales of  $\sim 10^9 M_\odot$  (Bode et al. 2001; Schneider et al. 2012; Anderhalden et al. 2012, 2013; Lovell et al. 2014). Modifying the abundance of halos at this mass scale will result in observable differences in the counts of dwarf galaxies around the Local Group and in the field in the low- $z$  Universe.

keV-scale sterile neutrinos represent a plausible dark matter candidate from a particle physics point-of-view (Dodelson & Widrow 1994; Shi & Fuller 1999; Asaka et al. 2005; de Gouvêa 2005). The recent detection of a possible line at 3.55 keV in the Perseus cluster (Bulbul et al. 2014; Boyarsky et al. 2014), stacked galaxy clusters (Bulbul et al. 2014), the Milky Way Galactic Center (Boyarsky et al. 2015), M31 (Boyarsky et al. 2014), and eight other clusters of galaxies at greater than  $2\sigma$  (Iakubovskiy et al. 2015), while contentious, has further heightened interest in keV-scale dark matter: the radiative decay of a 7.1 keV sterile neutrino would result in a 3.55 keV X-ray line. If this is indeed the origin of the line, it is the first non-gravitational signature of DM and is revolutionary. However, even in this case, the effects of such a particle on structure formation are *not* uniquely determined by its mass: different production mechanisms produce different momentum-space distributions of the sterile neutrino dark matter for particles of identical mass.

WDM models have often been categorized in two types (e.g. Colombi et al. 1996). “Early decoupled species” such as gravitinos, which are often referred to as “thermal” WDM, are produced in thermal equilibrium but decouple early (at

$T \gg 100 \text{ GeV}$ ); for such particles, the particle mass and decoupling temperature set the effect on large-scale structure. “Sterile neutrinos” often is used to mean right-handed neutrinos produced by oscillations produced at  $T \lesssim 1 \text{ GeV}$ . So long as  $g_*$  is unchanged during their production (and in the absence of any resonant production), one can derive a mapping between early decoupled species (thermal WDM) and oscillation-produced sterile neutrino dark matter (Colombi et al. 1996; Viel et al. 2005):

$$m(\nu_s) = 4.43 \text{ keV} \left( \frac{m_{\text{thermal}}}{1 \text{ keV}} \right)^{4/3} \left( \frac{\Omega_{\text{DM}} h^2}{0.1225} \right)^{-1/3}. \quad (1)$$

In the well-known Dodelson-Widrow (1994) model of sterile neutrinos produced via non-resonant oscillations, however,  $g_*$  *does* change during oscillation production. This change is particularly large during the quark-hadron transition, which alters production significantly (Abazajian & Fuller 2002). The applicability of Equation 1 to cosmological interpretations of the effects of sterile neutrinos is therefore not clear, a priori. Abazajian (2006) calculated the effects of the change of  $g_*$  through the quark-hadron transition and the effects of the commensurate neutrino opacity change. This results in a correction between equivalent particle masses for thermal early-decoupled WDM and non-resonant sterile neutrino WDM; the corrected relationship is given by

$$m(\nu_s) = 3.90 \text{ keV} \left( \frac{m_{\text{thermal}}}{1 \text{ keV}} \right)^{1.294} \left( \frac{\Omega_{\text{DM}} h^2}{0.1225} \right)^{-1/3}. \quad (2)$$

We have calculated this relation by matching the value of half-mode suppression between the non-resonant Dodelson-Widrow transfer functions calculated in Abazajian (2006) and the thermal WDM transfer functions, e.g., in Viel et al. (2005). Eq. 2 is accurate in the half-mode match to within 1% given the two transfer function relations. We note that while the difference in the normalization and exponent in the thermal mass term of Eq. 2 relative to Eq. 1 is small, this difference can have a significant ( $\sim 20\%$ ) effect on Dodelson-Widrow sterile neutrino mass constraints, particularly at larger particle masses that are currently being derived from constraints based on Lyman-alpha forest data (Baur et al. 2015). The cosmological effects of sterile neutrinos produced through early decoupling (e.g., Patwardhan et al. 2015) ac-

tually behave as thermal WDM in their transfer function and not as oscillation-produced transfer functions.

In the case of the Shi-Fuller (1999) sterile neutrino model of resonant production in the presence of a large lepton asymmetry, the momentum distributions are substantially non-thermal and their transfer functions need to be specifically calculated. The main effect of this non-thermal distribution is to modify the linear theory transfer function relative to thermal models. How this modification evolves in the nonlinear regime is not obvious and must be studied with numerical simulations, in general. Furthermore, as shown by Abazajian (2014) and Venumadhav et al. (2015), a large range of different behaviors are possible for a Shi-Fuller sterile neutrino of a given mass, with the mixing angle between sterile and ordinary neutrinos and cosmological lepton number determining on which scales power is suppressed. Neither Equation 1 nor Equation 2 applies to Shi-Fuller sterile neutrinos, therefore.

In this work, we explore a range of parameter space of the Shi-Fuller (resonantly-produced) sterile neutrino DM model that can account for 3.55 keV X-ray observations; our goal is to study the effects of such models on cosmological structure formation. Previous studies of the MW in a WDM cosmology focus only on thermal WDM particle models (Lovell et al. 2012; Kennedy et al. 2014; Lovell et al. 2014) or approximate resonant sterile neutrino DM with thermal WDM transfer functions (Bose et al. 2015). Approximations are used since calculating the exact transfer function for resonantly-produced sterile neutrino models, where particles are produced out of thermal equilibrium, is challenging, and differences between thermal and resonant sterile neutrino transfer functions appear small. Here, as was done in a companion work (Horiuchi et al. 2015), we use sterile neutrino transfer functions based on detailed Boltzmann code calculations and evaluate the relevance of thermal WDM approximations used to place constraints on sterile neutrino model parameter space.

The focus of this paper is two-fold. First, we examine the properties of Local Group galaxies using zoom-in, dissipationless  $N$ -body simulations for a variety of WDM models in order to explore solutions to CDM small-scale issues and predict distinguishable features of a WDM Local Group. Second, we determine the relevance of thermal WDM approximations to resonant sterile neutrino WDM models by comparing Local Group properties, DM halo mass functions in large cosmological volumes, and the 3D matter power spectrum at high-redshift.

The paper is organized as follows. In Section 2 we describe the WDM models evaluated in this work, the numerical simulation details, and analysis methods. We present our results for the Local Group simulations in Section 3 and field halo velocity functions of cosmological volume simulations in Section 4. We give the high-redshift matter power spectrum results of the cosmological volume simulations in Section 5. In Section 6 we discuss our results and present our conclusions.

## 2 SIMULATIONS

Throughout this work, we consider Shi-Fuller resonantly-produced sterile neutrino DM models with a particle mass

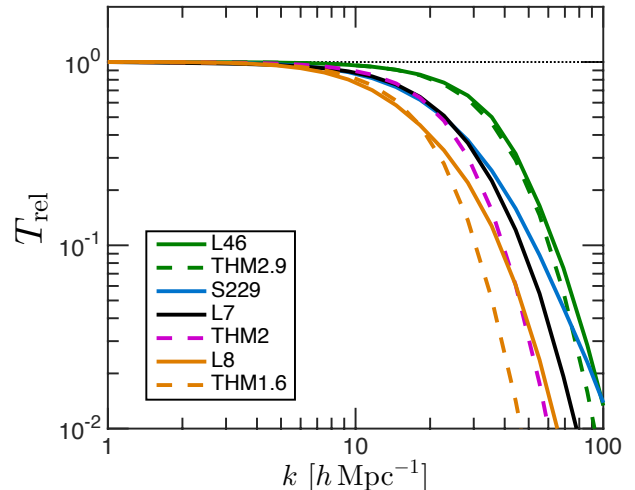


**Figure 1.** Suppression of the linear matter power spectrum of resonantly-produced sterile neutrino models (solid lines) and their best-fit thermal equivalent model (dashed lines) relative to CDM, where  $T_{\text{rel}} = \sqrt{P_{\text{WDM}}/P_{\text{CDM}}}$ . The L46 (solid; green), L7 (solid; black), and L8 (solid; orange) models are based on the sterile neutrino DM production calculations of Abazajian (2014), while S229 (solid; blue) model is based on the more accurate treatment of Venumadhav et al. (2015). The L7 and S229 models both share an equivalent thermal WDM model of  $m = 2$  keV (THM2/dashed; magenta). The shape and large- $k$  behavior of the WDM transfer functions vary among the sterile neutrino models and compared with their thermal equivalent models.

of  $m_\nu = 7.1$  keV that are consistent the observed 3.55 keV line. As described in the Section 1, the particle mass does not uniquely specify the effect such a particle has on structure formation. We examine a range of sterile neutrino parameters that modify the linear matter power spectrum on scales relevant to small-scale structure formation. We additionally consider two calculations of Shi-Fuller models based on the work of Abazajian (2014; hereafter, A14) and also the more recent results of Venumadhav (2015; hereafter, V15).

The A14 models are parametrized by  $L$ , the lepton number of the Universe (relative to the photon number) prior to resonant production. We consider the models discussed in A14 of  $L = 4.6 \times 10^{-4}$ ,  $7 \times 10^{-4}$ , and  $8 \times 10^{-4}$  (hereafter, L46, L7, and L8). These models bracket the region of parameter space that is consistent with producing the 3.55 keV line and suppresses the linear matter power spectrum on small-scales that are relevant for DM halo counts, as it relates to the Missing Satellites Problem. Once  $m_\nu$  is fixed and the lepton number is specified, the mixing angle  $\sin^2(2\theta)$  is also determined. The case of L7 has a mixing angle of  $\sin^2(2\theta) \approx 3 \times 10^{-11}$ , for example.

The models from V15 include a more complete treatment of the redistribution of lepton number and opacity of active neutrinos. We consider three V15 models parameterized by their mixing angles:  $\sin^2(2\theta) = \{0.8, 2.9, \text{ and } 20\} \times 10^{-11}$  (hereafter, S208, S229, and S220). The V15 models are selected to bracket the region of sterile neutrino parameter space that is consistent with the candidate radiative decay line observations and have a similar half-mode suppression

**Table 2.** Host halo properties. *Column 1:* Model label; *Column 2:* Host halo virial mass; *Column 3:* Virial radius; *Column 4:* Maximum circular velocity; *Column 5:* Radius of circular velocity maximum; *Column 6:* Separation between host halos; *Column 7:* Number of halos above resolution limit; *Column 8:* Number of halos above the artificial fragmentation limit.

Model	$M_{\text{vir}}$ [ $h^{-1} M_{\odot}$ ]	$R_{\text{vir}}$ [ $h^{-1} M_{\odot}$ ]	$V_{\text{max}}$ [ $\text{km s}^{-1}$ ]	$R_{\text{max}}$ [ $h^{-1} \text{kpc}$ ]	$\Delta$ [ $h^{-1} \text{kpc}$ ]	$N(> 8 \text{ km s}^{-1})$	$N(> 15 \text{ km s}^{-1})$
CDM (Thelma)	$1.05 \times 10^{12}$	256.69	171.48	61.69	623.7114	468	69
CDM (Louise)	$8.50 \times 10^{11}$	239.52	158.82	33.07	623.7114	463	70
L46 (Thelma)	$1.04 \times 10^{12}$	256.44	172.08	60.21	657.6297	101	38
L46 (Louise)	$8.50 \times 10^{11}$	239.56	156.83	29.74	657.6297	106	37
L7 (Thelma)	$1.04 \times 10^{12}$	256.30	171.03	60.81	665.3431	55	23
L7 (Louise)	$8.47 \times 10^{11}$	239.22	153.69	25.26	665.3431	53	18
THM2 (Thelma)	$1.05 \times 10^{12}$	256.76	170.99	61.23	663.9513	48	26
THM2 (Louise)	$8.44 \times 10^{11}$	238.96	155.72	26.18	663.9513	48	17
S229 (Thelma)	$1.05 \times 10^{12}$	256.62	170.89	65.4	661.1437	59	26
S229 (Louise)	$8.49 \times 10^{11}$	239.39	154.65	25.36	661.1437	56	19
L8 (Thelma)	$1.05 \times 10^{12}$	256.71	171.63	62.97	662.5239	36	21
L8 (Louise)	$8.43 \times 10^{11}$	238.88	156.51	25.22	662.5239	30	11

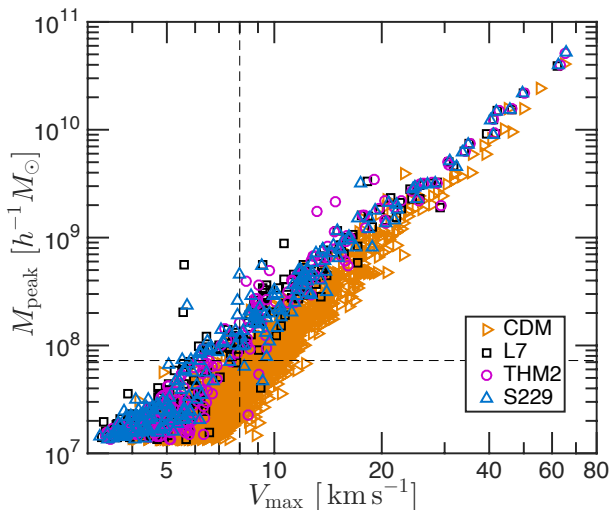


**Figure 2.** The peak mass of CDM and WDM Local Group field halos with respect to  $V_{\text{max}}$  at  $z = 0$ . For a fixed peak mass bin, the WDM halos have a smaller  $V_{\text{max}}$  value, indicating a lower central density. The three WDM models shown here (L7, THM2, and S229) have the same half-mode suppression scale. Their Local Group field halo sets shown here have a similar distribution in  $M_{\text{peak}} - V_{\text{max}}$  space. The vertical dashed-line shows the convergence limit of the simulation of  $V_{\text{max}} = 8 \text{ km s}^{-1}$  and the horizontal dashed-line gives the limiting mass  $M_{\text{lim}}$  as defined by Lovell et al. (2014), below which the halos may have formed via artificial fragmentation. Only a few points fall in the bottom-right section as delineated by the dashed lines, indicating that our results are robust against discreteness effects.

scale as the three A14 models. The lepton number (or equivalently here, the mixing angle) determines the resonantly-produced sterile neutrino momentum distribution and therefore the suppression of the linear matter power spectrum. For example, the L7 and S229 have similar values of  $\sin^2(2\theta)$ .

These models are therefore comparable through their suppression of the linear matter power spectrum. Figure 1 shows the ‘relative’ transfer function,  $T_{\text{rel}} = \sqrt{P_{\text{WDM}}/P_{\text{CDM}}}$ , that describes the suppression of the linear matter power spectrum relative to CDM for these models. The  $T_{\text{rel}}$  of the L7 and S229 models in Figure 1 show a similar degree of suppression relative to CDM down to large values of  $k$  where  $T_{\text{rel}} > 0.1$ , albeit with a slightly different shape.

Each relative transfer function can be fit by a comparable relative transfer function for a thermal WDM model, which we subsequently refer to as its ‘thermal equivalent’. The L7 and S229 cases have a thermal equivalent model of  $m = 2 \text{ keV}$  (THM2), while the L46 (L8) thermal equivalent particle mass is higher (lower). The effective ‘warmth’ of the sterile neutrino models is then represented by the scale where the linear matter power spectrum diverges from CDM matter power spectrum, where warmer models suppress power on larger scales. Importantly, despite representing the best-fit case, the momentum distributions of the thermal equivalent models result in relative transfer functions that have different shapes from their sterile neutrino counterparts, as shown in Figure 1. We explore this point in detail throughout this work.

The thermal equivalent transfer functions of our fiducial L7 and S229 models match closely at the half-mode scale ( $k_{1/2}$ ), where  $T_{\text{rel}}(k_{1/2}) = 0.5$ , as is shown in Fig. 1. The half-mode scale indicates where free-streaming effects are significant, having suppressed the linear matter power spectrum by 50% (Avila-Reese et al. 2001). The half-mode mass is defined as

$$M_{1/2} = \frac{4\pi}{3} \left( \frac{\lambda_{1/2}}{2} \right)^3 \bar{\rho}, \quad (3)$$

where  $\lambda_{1/2} = 2\pi/k_{1/2}$ .

We conduct two simulation suites. The first are a set of zoom-in, dark-matter-only  $N$ -body simulations that are based on a single realization of a Local Group from the Exploring the Local Volume In Simulations (ELVIS) suite (Garrison-Kimmel et al. 2014a). The ELVIS suite is a se-

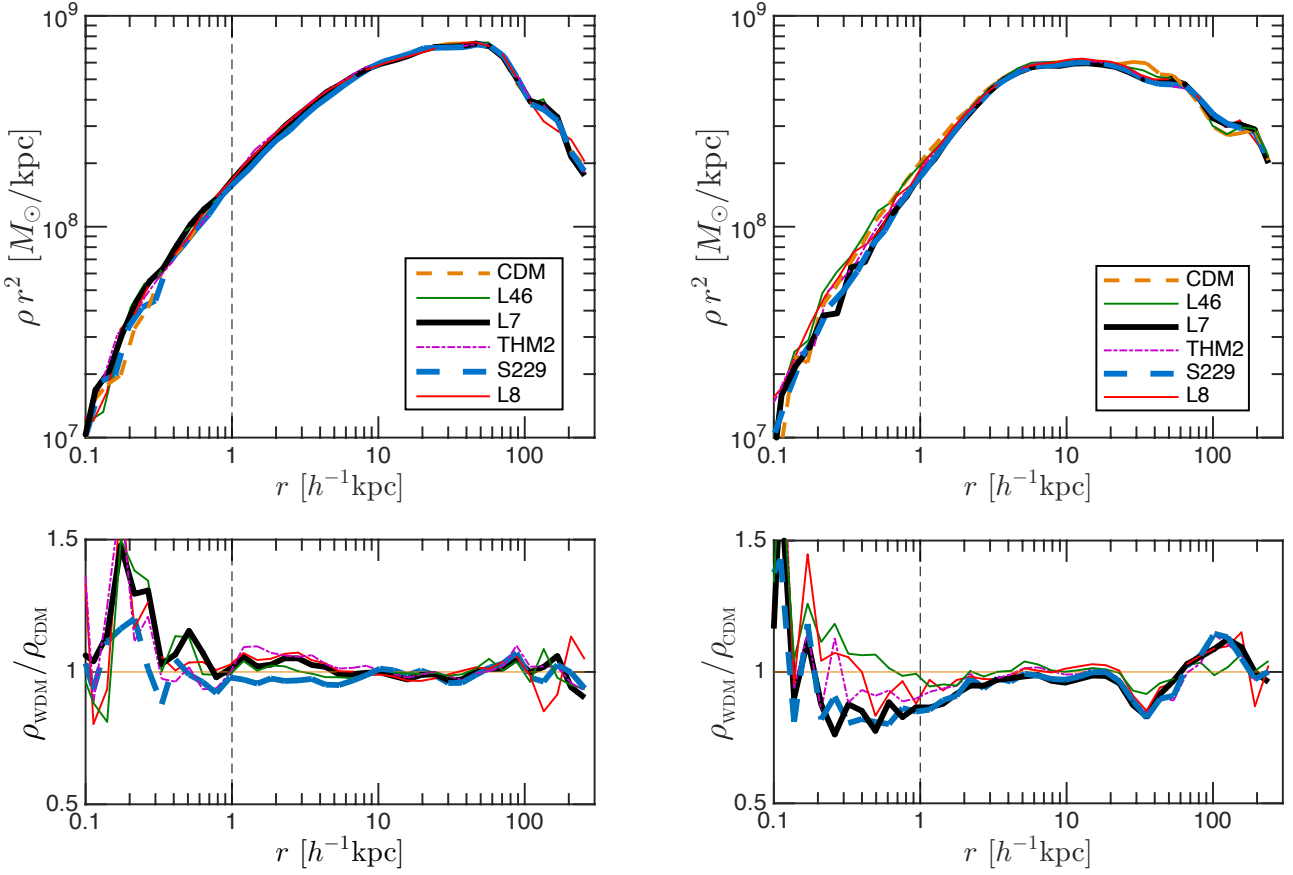


**Figure 3.** The density profiles (top row) and ratio of WDM and CDM density profiles (bottom row) of host halos Thelma (left column) and Louise (right column) for the CDM (orange;dashed) and WDM models: L7 (black; thick-solid), THM2 (magenta; dot-dashed), L46 (green; thin-solid), L8 (red; thin-solid), S229 (blue; dashed). The dashed-vertical line marks the largest convergence radius ( $r = 1 h^{-1} \text{kpc}$ ) based on the criterion of Power et al. (2003) as determined by the AHF halo finder (Knollmann & Knebe 2009). Differences for  $r < 1 h^{-1} \text{kpc}$  are likely due to lack of numerical convergence. The density profiles for each model are very similar over the full radial range of each host. Small variations in the outer density profiles come from individual massive substructures.

ries of high-resolution  $N$ -body simulations of 48 Milky Way-sized DM halos (24 in Local Group-like pairs, 24 isolated halos) in a  $\Lambda$ CDM cosmology. The paired halos are selected to be representative of the Local Group by resembling the Milky Way and M31 in mass, separation, relative kinematics, and their  $\sim 2$  Mpc scale environment. The “Thelma and Louise” Local Group from the ELVIS suite was chosen to be the representative Local Volume targeted in this work. The Local Group zoom-in simulations are run for four of the sterile neutrino WDM models discussed above (L46, L7, L8, and S229) and a thermal  $m = 2$  keV WDM model. These simulations are compared to the original CDM simulation from the ELVIS suite. The three A14 models are selected to bracket a range of linear matter power suppression, as shown in Figure 1, that is predicted to resolve the Missing Satellites Problem. The S229 and THM2 models, as discussed above, are directly comparable to the L7 model and facilitate an exploration of the relative transfer function shape on Local Group properties.<sup>1</sup>

<sup>1</sup> A related work by Horiuchi et al. (2015) compares zoom-in simulations of an isolated MW-sized DM halo for the V15 models

The Tree-PM  $N$ -body code Gadget-3, an updated version of the public Gadget-2 code (Springel 2005), was used to perform the simulations, which assume a WMAP7 cosmology:  $\Omega_m = 0.266$ ,  $\sigma_8 = 0.801$ ,  $\Omega_\Lambda = 0.734$ ,  $n_s = 0.963$ , and  $h = 0.71$  (Larson et al. 2011). The particle mass of the high-resolution zoom-in region is  $m_p = 1.3 \times 10^5 h^{-1} M_\odot$ , which gives an effective resolution of  $4096^3$  for the high-resolution region. The simulations start at an initial redshift of  $z_i = 125$  and employ a Plummer-equivalent softening of  $\epsilon = 1 h^{-1} \text{kpc}$ , which is constant in comoving units until  $z = 9$ , where it becomes fixed at  $\epsilon = 100 h^{-1} \text{pc}$  (physical) to redshift zero. The initial conditions for the simulation were set-up using the MUSIC code (Hahn & Abel 2011).

Our second suite of simulations are homogeneously-resolved, cosmological volume dark-matter-only simulations of  $N_p = 512^3$  particles in cubic volumes of box length  $L = 25 h^{-1} \text{Mpc}$  with a WMAP7 cosmology. We simulate the

S208, S229, and S220 with observations of the Local Group satellites specifically to determine sterile neutrino model resolutions to the Missing Satellites and Too Big To Fail problems.

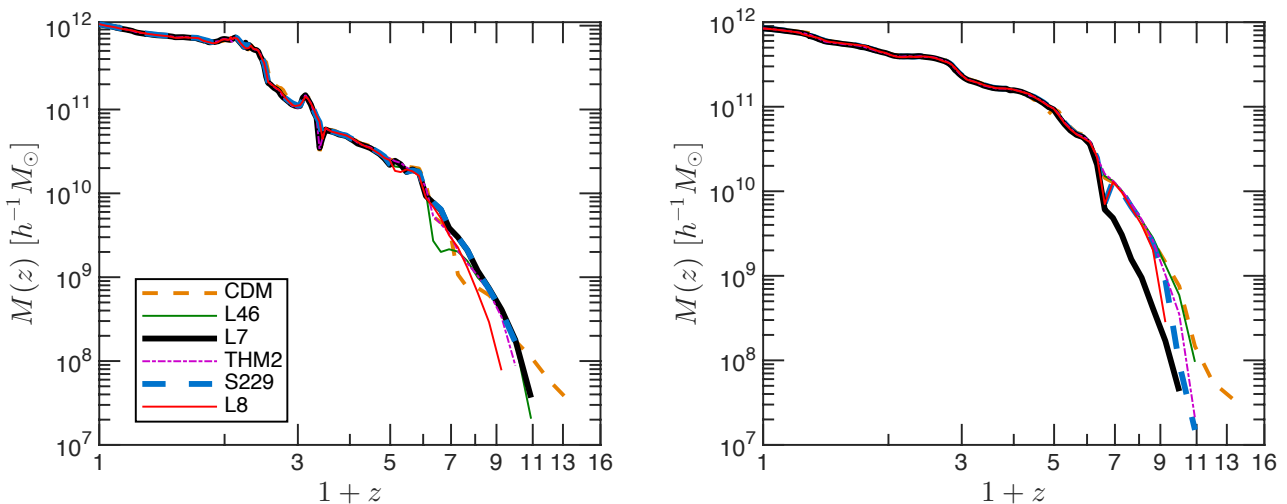


**Figure 4.** The mass assembly histories of host halos Thelma (left panel) and Louise (right panel) for the DM models: L7 (black; thick-solid), THM2 (magenta; dot-dashed), L4.6 (green; thin-solid), L8 (red; thin-solid), S229 (blue; dashed), CDM (orange; dashed). After a redshift of  $z = 5$  the virial mass evolution of each halo is identical for each DM model. Prior to  $z = 5$ , there are small departures from a common assembly history that are not correlated with WDM model warmth. The host halos masses at initial collapse are near (or below) the half-mode mass of each WDM model (listed in Table 1). The random departures from the early common assembly history are likely related to the mass build-up of halos near the different models’ half-mode scales, where free-streaming effects are relevant.

A14 (L46, L7, L8) and V15 (S220, S229, S208) sterile neutrino WDM models and their best-fit thermal WDM models ( $m = 1.6, 2,$  and  $2.9$  keV; hereafter, THM1.6, THM2, and THM2.9). The Plummer-equivalent force softening for these simulations,  $\epsilon = 1.25 h^{-1}$  kpc, is constant in comoving units for the duration of the simulation. The simulations start at  $z_i = 125$ . The L7, THM2, S229, and CDM simulations were evolved to  $z = 0$ ; the L46, L8, S208, and S220 models were simulated to understand halo properties at high redshift and were therefore terminated at  $z = 2$ . The nonlinear matter power spectrum of each simulation was calculated using the ProCorr code (Obreschkow et al. 2013).

We use the Amiga Halo Finder (AHF) (Knollmann & Knebe 2009) to identify self-bound dark matter halos. The virial mass of a dark matter halo,  $M_{\text{vir}}$ , is defined as the mass contained within a sphere out to the virial radius,  $R_{\text{vir}}$ , where the density of the halos is 200 times the mean density of the universe. We define  $R_{\text{max}}$  as the radius where the maximum velocity,  $V_{\text{max}}$ , of the circular velocity profile,  $V_c(r) = \sqrt{GM(<r)}/r$ , is reached for a dark matter halo at redshift zero. The assembly histories of the dark matter halos are determined by the MergerTree code that is included in AHF. The maximum circular velocity of a dark matter halo over its entire assembly history is defined as  $V_{\text{peak}}$ . Halo partners across different simulations are also identified using the AHF MergerTree code by finding the corresponding halo that shares the most particles with the same Gadget-3 Particle IDs. For example, Halo A in the CDM simulation is considered a partner halo of Halo B in the L7 WDM simulation if both halos maximize the function  $N_{AB}^2/(N_A N_B)$ , where  $N_{AB}$  is the number of shared particles in each halo,  $N_A$  is the number of particles in halo A, and  $N_B$  is the number of particles in halo B. This criterion is determined for halos in each simulation type with respect to every other simulation type and then compared for overlap

between simulation types. When comparing halos directly across different simulation types, we do not include halos that fail this criterion, even if the halos satisfy a separate selection criteria (such as a range of halo masses).

The formation of halos below the free-streaming scale in WDM should be highly suppressed; however, WDM numerical simulations find an excess of low-mass halos compared to expectations both from theory and in comparison to CDM, where the CDM linear matter power spectrum has significantly more power than WDM. These halos in WDM are numerical artifacts resulting from fragmentation of filaments induced by discreteness noise and exist whether the initial particle load is grid-based or glass-based (Wang & White 2007). Two methods that address this issue of spurious halos are: removing halos below a limiting mass and shape criterion as defined by Lovell et al. (2014), or considering only halos with a mass far above the mass scale where spurious halo formation is a significant problem. In this work, we take the latter approach.

We note, however, that the contamination from spurious halos is likely to be small even at the resolution limit of our Local Group simulation ( $V_{\text{max}} > 8 \text{ km s}^{-1}$ ). Figure 2 shows the relationship of the peak mass,  $M_{\text{peak}}$  to  $V_{\text{max}}(z = 0)$  of Local Group field halos in the CDM, L7, S229, and THM2 simulations. The vertical and horizontal dashed lines show the resolution limit at  $V_{\text{max}} = 8 \text{ km s}^{-1}$  and the limiting mass, defined as  $M_{\text{lim}} = 10.1 \bar{\rho} d k_{\text{peak}}^{-2}$  (Wang & White 2007), respectively. We follow Lovell et al. (2014) and multiply this value by  $\kappa = 0.5$  in order to best account for the mass scale below which artificial fragmentation dominates to obtain a value of  $M_{\text{lim}} = 7.25 \times 10^7 M_{\odot}/h$ . Halos in the bottom right quadrant of Figure 2 are halos that are above our resolution limit, but below the limiting mass, where their formation may have been the result of artificial fragmentation. The small number of points in this section of

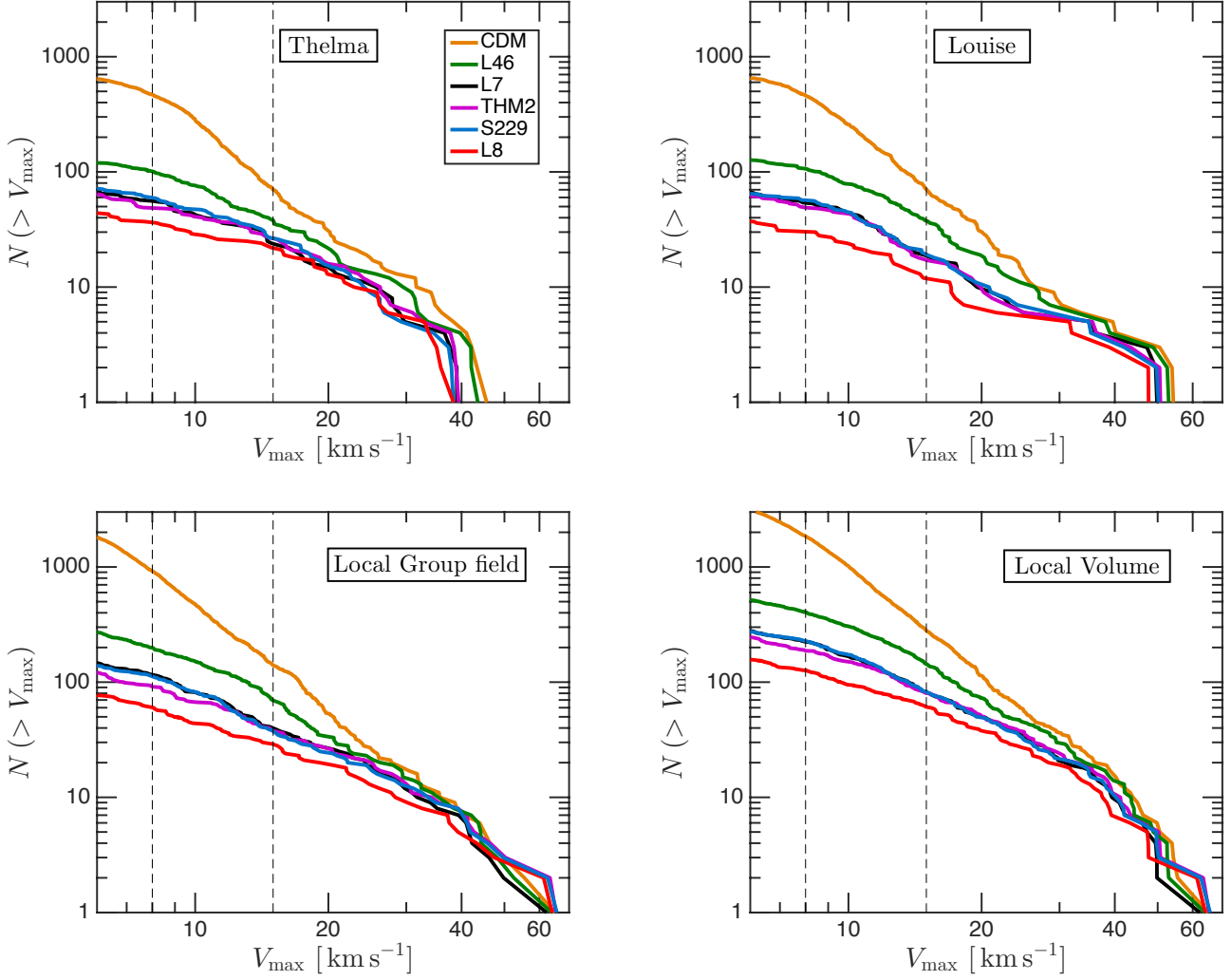


**Figure 5.** The cumulative subhalo  $V_{\max}$  function for hosts Thelma (top left panel) and Louise (top right panel), the Local Group field halos (bottom left panel), and all Local Volume halos including host subhalos and field halos (bottom right panel) for each DM model. The convergence limit of  $V_{\max} = 8 \text{ km s}^{-1}$  and artificial fragmentation limit of  $V_{\max} = 15 \text{ km s}^{-1}$  are respectively represented by the dashed-vertical lines. The five WDM models suppress the number of subhalos at each mass relative to CDM.

the figure illustrates that our results are not strongly contaminated by artificial fragmentation. However, when considering the internal properties of DM halos, we base our conclusions on halos with  $V_{\max} > 15 \text{ km s}^{-1}$ , which we define as our “artificial fragmentation limit”. This is a very conservative choice that selects halos with an  $M_{\text{peak}}$  value significantly above  $M_{\text{lim}}$ , as shown in Figure 2. We quote results for halos with  $V_{\max} > 8 \text{ km s}^{-1}$  where appropriate.

### 3 THE LOCAL GROUP

#### 3.1 Local Group host halos

The general properties of the Thelma and Louise host halos at redshift zero (e.g., the virial mass, virial radius, physical separation) are similar for each DM model considered here. The values for these halo properties (among others) can be found in Table 2 for each DM model. The general make-up

of the host halos are unaffected by the relative warmth of the respective WDM models.

The spherically-averaged density profiles and ratios of the WDM to CDM density profiles for the Thelma and Louise host halos at  $z = 0$  are shown in Figure 3. The density profiles for each host show good agreement for all DM models at all radii. The ratios of the WDM and CDM hosts’ density profiles show only small departures from unity on most scales. The larger variations near the virial radius in the Louise hosts’ DM density profiles is due to variations in the radial distribution of large substructures. Inside the resolution limit of  $r = 1 h^{-1} \text{ kpc}$ , the density ratios show strong fluctuations that are likely the result of numerical effects.

We have also investigated the shape of both host halos in the CDM, L7, THM2, and S229 models by comparing the ratios of the minor and intermediate halo axes relative to the major halo axis. The host halos shapes are triaxial at all radii with some variation in shape with radius. The

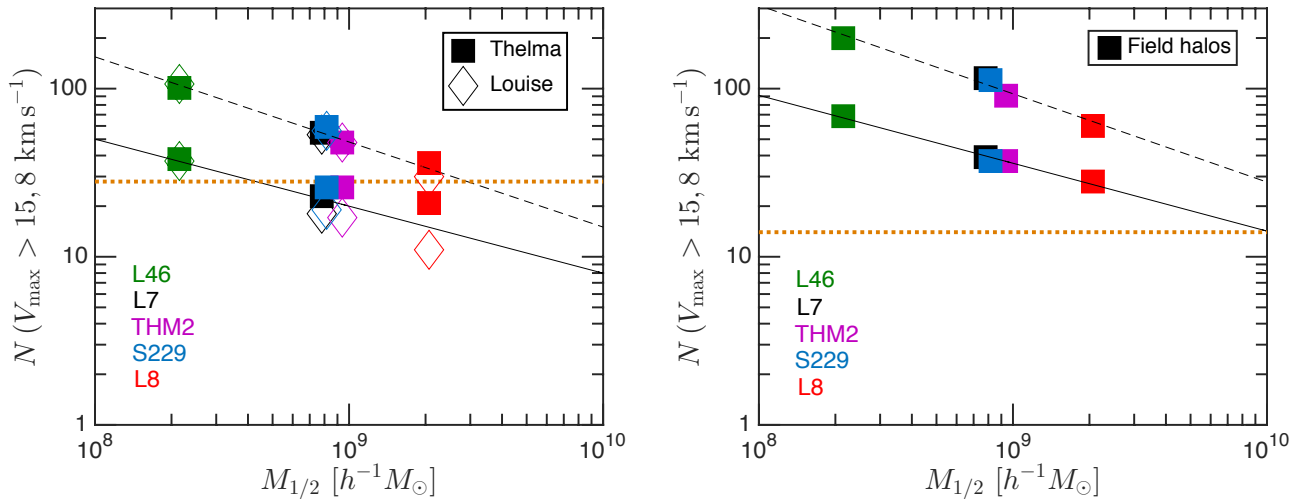


**Figure 6.** The cumulative number of subhalos above a cutoff velocity in the cumulative subhalo  $V_{\max}$  functions for hosts Louise and Thelma (left panel) and the Local Group field halos (right panel) with respect to the half-mode mass (defined in the text and listed in Table 1). In the left panel, the solid squares (opened diamonds) represent Thelma (Louise) subhalo abundances for DM models: L7 (black), THM2 (magenta), L4.6 (green), L8 (red), and S229 (blue). The solid (dashed) black line gives the power law fit for a cut of  $V_{\max} = 15$  (8)  $\text{km s}^{-1}$ . The number of DM subhalos in each host halo and in the Local Group field is well-predicted by the half-mode mass of the relative transfer functions. The orange, dotted horizontal lines show the count of MW satellite galaxies (left; Horiuchi et al. 2015) and Local Group field galaxies (right; McConnachie 2012). The L8 model is in tension with the current count of MW satellite galaxies.

DM model type does not affect the host halo shape as there are no significant differences in the Thelma and Louise axis ratios at any radius between CDM and WDM models.

The mass assembly histories of the host halos for each DM model are shown in Figure 4. After a redshift of  $z = 5$ , both host halo assembly histories are identical for all DM models. Prior to  $z = 5$ , the hosts’ assembly histories diverge for each DM model. Although the WDM model hosts collapse later than in the CDM model, there is not a correlation between the WDM model warmth and the initial collapse time nor with the subsequent mass build-up leading up to the common assembly history of  $z < 5$ . The host halo mass for each WDM model at the time of initial collapse is near or below the half-mode mass,  $M_{1/2}$ , (as listed in Table 1) where free-streaming effects that suppress structure formation are significant. The early mass assembly of the host halos are then likely built up from the merging of halos with masses on the order of  $M_{1/2}$ . The model-dependent nature of this mass scale then accounts for the differences in the initial collapse times and early mass assembly history of the different DM model host halos shown in Figure 4.

### 3.2 Local Group Halo Abundances

The cumulative  $V_{\max}$  functions for Thelma and Louise subhalos, Local Group field halos (located within 1.2 Mpc of either host center, but outside both host virial radii), and a Local Volume set (all DM halos within 1.2 Mpc of either host center) are shown in Figure 5. The CDM model predicts hundreds of subhalos within each host’s virial radius and thousands in the Local Group down to the resolution limit of  $V_{\max} \geq 8 \text{ km s}^{-1}$ . The Thelma, Louise, Local Group field, and Local Volume cumulative  $V_{\max}$  functions for the

WDM models are reduced relative to the CDM cumulative  $V_{\max}$  function at all masses to a degree that depends on the warmth of the model; warmer models have a lesser number of subhalos relative to CDM. The relative suppression in the WDM cumulative  $V_{\max}$  functions is more pronounced at the low-mass end where the strong suppression in the small-scale power of the transfer functions in Figure 1 results in greatly reduced low-mass halo formation. For example, the L7 model cumulative  $V_{\max}$  functions are reduced by a factor of ten relative to CDM at the resolution limit, even without removing artificial subhalos.

The cumulative subhalo  $V_{\max}$  functions of both host halos show a strong similarity between L7 and S229 sterile neutrino models and their thermal equivalent  $m = 2 \text{ keV}$  WDM model over the full  $V_{\max}$  range. There are small differences, on the order of 10% – 20%, between the sterile neutrino and thermal equivalent models’ low-mass subhalo abundances near the resolution limit. The Local Group and Local Volume  $V_{\max}$  functions also find a slightly greater number of low-mass DM halos ( $\sim 20\%$ ) for the sterile neutrino models than their thermal equivalent model. We caution, however, that these differences are not only near the resolution limit of the simulations, but also set in for  $V_{\max} < 15 \text{ km s}^{-1}$ , where artificial fragmentation may remain an issue. The relevance of this difference in the low-mass halo abundance as it relates to satellite galaxy counts in the MW and M31 are discussed in detail by Horiuchi et al. (2015).

Figure 6 illustrates the relationship between the half-mode mass ( $M_{1/2}$ ), the halo mass scale where free-streaming effects are significant, and the total number of halos in the  $V_{\max}$  function above a cutoff velocity. We consider the total number of halos above the cuts of  $V_{\max} \geq 8 \text{ km s}^{-1}$  and  $V_{\max} \geq 15 \text{ km s}^{-1}$ . We fit the points in each panel of Fig. 6

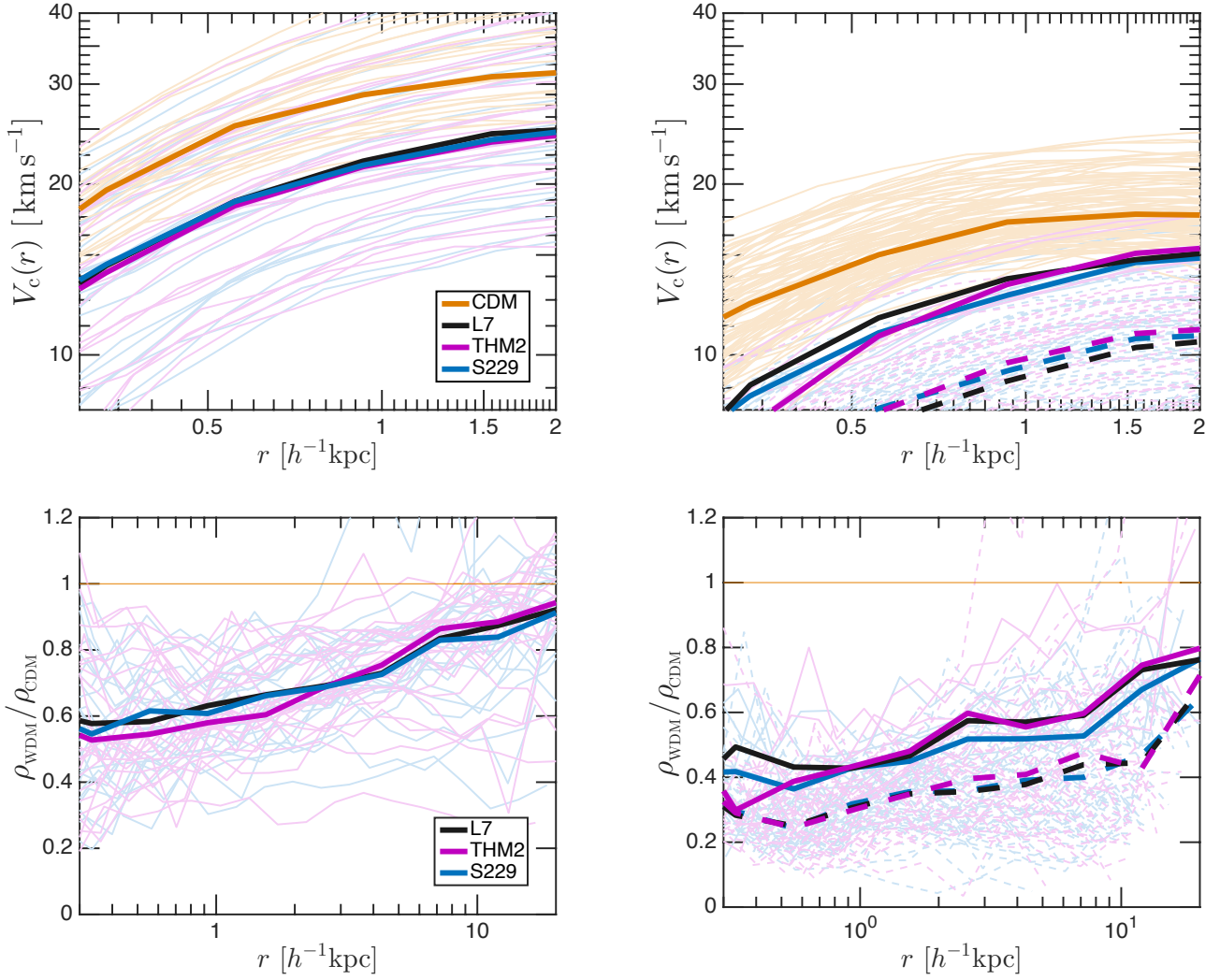


**Figure 7.** The rotation curves (top row) and density ratios (bottom row) of the Local Group field halos for the CDM (orange), S229 (blue), and THM2 (magenta) DM models. WDM field halos with  $V_{\text{max}} > 15 \text{ km s}^{-1}$  are shown as solid curves and those with  $8 < V_{\text{max}} < 15 \text{ km s}^{-1}$  are dashed. The thick dark curves give the median values of each DM model halo set: solid for halos with  $V_{\text{max}} > 15 \text{ km s}^{-1}$  and dashed for  $V_{\text{max}} > 8 \text{ km s}^{-1}$ . The median relations of L7 halos show a 40% reduction in the median central density relative to CDM halos with  $V_{\text{max}} > 25 \text{ km s}^{-1}$  (bottom left panel), and a corresponding  $\sim 5 \text{ km s}^{-1}$  reduction in the median rotation curves (top left panel). Lower mass WDM halos (right panels) show a more pronounced decrease in the median density ratios of 60–70% in the central  $1 h^{-1} \text{ kpc}$  and 20–30% near the halos’ virial radius (although with significant scatter). Including halos with  $8 < V_{\text{max}} < 15 \text{ km s}^{-1}$  results in a more pronounced reduction in the WDM median density ratio and rotation curve relative to CDM.

to a power law relation,  $y \propto x^n$ , where  $n = -0.40$  ( $-0.51$ ) for the combined subhalo set of Thelma and Louise for  $V_{\text{max}} > 15$  ( $8$ )  $\text{km s}^{-1}$ , and  $n = -0.40$  ( $-0.53$ ) for the field halos in the Local Group.

The half-mode mass is strongly predictive of the total number of subhalos in both hosts combined (left panel) and in the Local Group (right panel) for both  $V_{\text{max}}$  cuts. The subhalo mass function dependence on the filtering mass was previously studied in Dunstan et al. 2011 for non-resonant WDM models. The power law trends of the host subhalo sets and the Local Group field halos are very similar. Warmer WDM models show a larger dispersion around the power-law fit for Thelma and Louise subhalo abundances. This is

likely due to the small number of subhalos in the warmer models, since the variation around the trend is stronger for the larger  $V_{\text{max}}$  cut and the trend in Local Group for the larger  $V_{\text{max}}$  cut is the same as the subhalo set. The slight difference in the half-mode mass between thermal and sterile neutrino models results in a small difference in the total number of halos near the resolution limit in each host and in the Local Group.

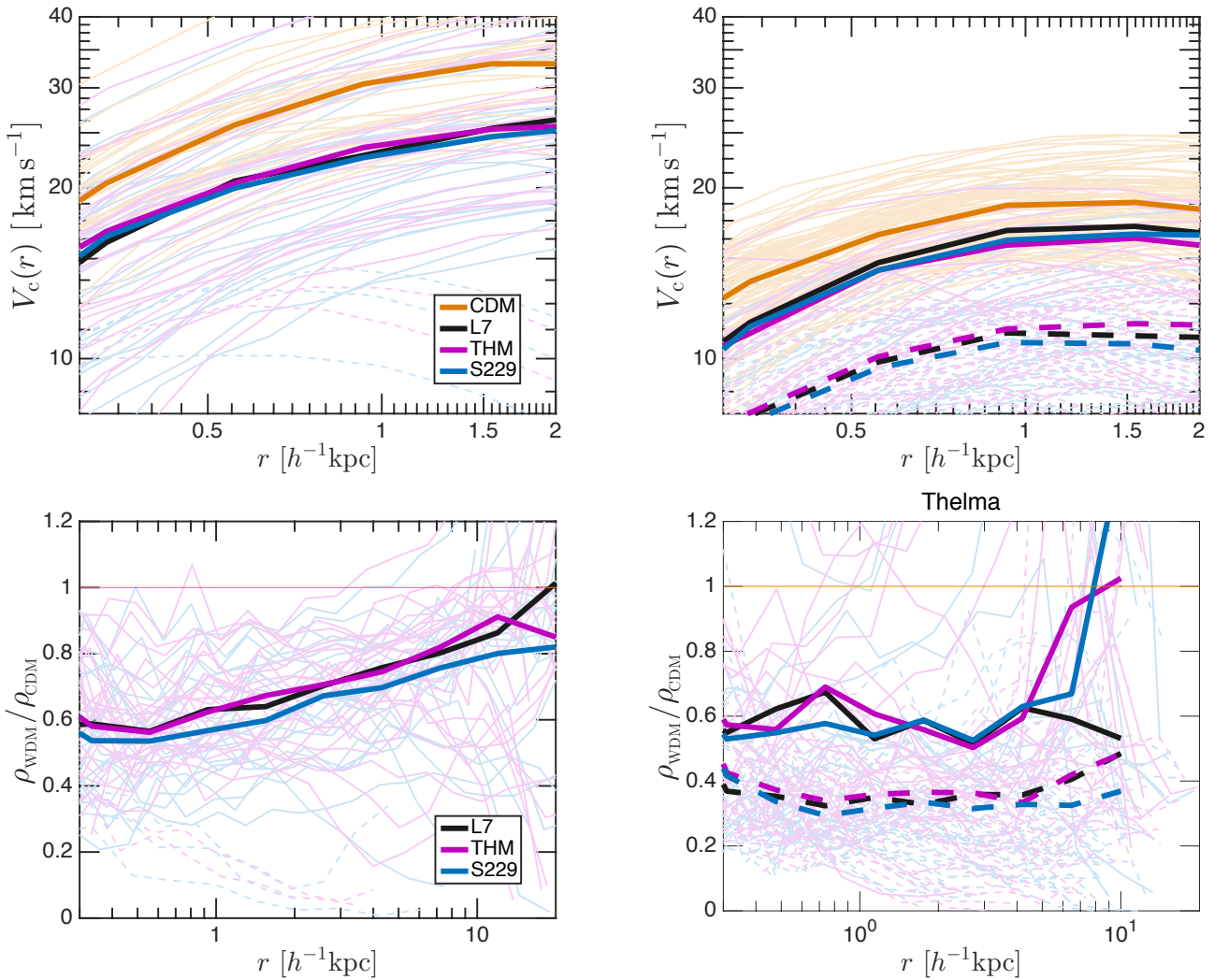


**Figure 8.** The rotation curves (top row) and density ratios (bottom row) of the Thelma and Louise subhalos for the CDM (orange), S229 (blue), and THM2 (magenta) models. The same selection criteria and median curve styles as described Figure 7 are used, with the exception of the bottom right panel, where the median density ratios are determined to  $r < 10 h^{-1} \text{ kpc}$ . The median rotation curves and density ratios of the  $V_{\text{max}} > 25 \text{ km s}^{-1}$  subhalos (left column) are quantitatively similar to the Local Group field results shown in Figure 7. The WDM subhalos counterparts to CDM subhalos with  $15 < V_{\text{max}} < 25 \text{ km s}^{-1}$  (right panels) show a 40% reduction in the median central density relative to CDM, if only WDM subhalos with  $V_{\text{max}} > 15 \text{ km s}^{-1}$  are considered. There are only  $\sim 10$  of these subhalos in each set and there is considerable scatter around the median that is likely due to tidal stripping effects in both WDM and CDM subhalos. Including subhalos with  $V_{\text{max}} > 8 \text{ km s}^{-1}$  lowers the median density ratio and rotation curve relative to CDM, bringing them into better agreement with Local Group field halo results.

### 3.3 Local Group Subhalo and Field Halo Internal Structure

We next consider the internal structure of the Local Group field halos and Thelma and Louise subhalos. The rotation curves and density profile ratios of WDM relative to CDM halos for the S229, L7, and THM2 Local Group field halos are shown in Figure 7. We also determine the median rotation curves and median density profile ratios for each DM model halo set (thick, dark curves). For simplicity, the individual L7 halo curves are not shown (although the median values of the L7 sets are presented). The halo sets were selected by, first, identifying all CDM Local Group field halos (located within 1.2 Mpc of either host center, but outside

both host virial radii). CDM Local Group field halos are then divided into two mass bins: halos with  $V_{\text{max}} > 25 \text{ km s}^{-1}$  (left column panels) and  $15 < V_{\text{max}} < 25 \text{ km s}^{-1}$  (right column panels). We then identify WDM Local Group field halo counterparts to these CDM halos that satisfy the halo correlation criterion described in Section 2.

The WDM halo counterparts are required to also be located in the Local Group field, but not to follow the  $V_{\text{max}}$  cuts given above, i.e. a WDM halo counterpart could be significantly more or less massive than the corresponding CDM halo. The THM2 and S229 WDM model rotation and density ratio curves, shown in Figure 7, are solid for halos with  $V_{\text{max}} > 15 \text{ km s}^{-1}$  and dashed for halos

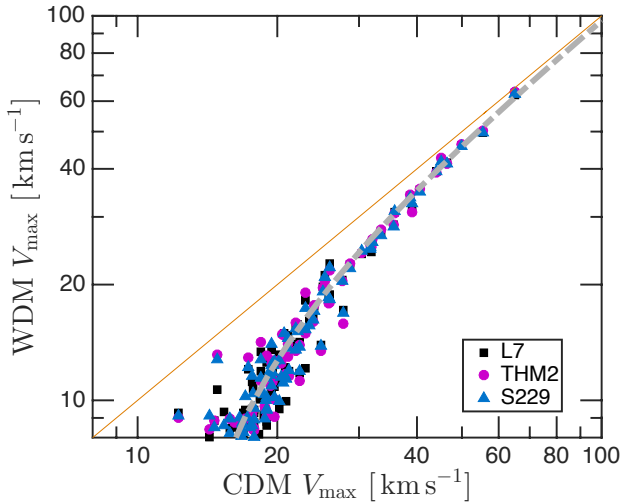


**Figure 9.** The WDM  $V_{\max}$  as a function of the matched CDM  $V_{\max}$  on a halo-by-halo basis for Local Group field halos. The different WDM model halos (L7 - black; S229 - blue; THM2 - magenta) have a similar distribution that bends away from the a one-to-one relation (orange curve) with CDM halos for smaller halo masses, as a result of reduced central densities in the WDM halos. The gray curve shows a fit to the points that includes all WDM model halos. Fits to individual WDM model halo sets (not shown) are similar to the fit for all WDM model halos.

with  $8 < V_{\max} < 15 \text{ km s}^{-1}$ . The CDM field halos with  $V_{\max} > 25 \text{ km s}^{-1}$  (left column) have all WDM halo counterparts with  $V_{\max} > 15 \text{ km s}^{-1}$ . For CDM field halos with  $15 < V_{\max} < 25 \text{ km s}^{-1}$  (right column), however, only a handful of WDM halo counterparts have a  $V_{\max} > 15 \text{ km s}^{-1}$ ; most have a  $V_{\max}$  value of  $8 < V_{\max} < 15 \text{ km s}^{-1}$ . Since the majority of WDM counterparts to the CDM field halos with  $15 < V_{\max} < 25 \text{ km s}^{-1}$  have a  $V_{\max}$  value below the artificial fragmentation limit, we plot the median rotation curve and median density profile ratio for WDM counterparts with  $V_{\max} > 15 \text{ km s}^{-1}$  (thick, solid curves) and for WDM halos with  $V_{\max} > 8 \text{ km s}^{-1}$  (thick, dashed curves) in the right column panels of Figure 7. While the WDM halo sets with  $V_{\max} > 8 \text{ km s}^{-1}$  are possibly contaminated by artificial fragmentation, they represent the majority of WDM counterparts to the CDM field halos in the low-mass bin. If artificial fragmentation is not significant, then the WDM field halos with  $V_{\max} > 8 \text{ km s}^{-1}$  are the appropriate comparisons to CDM field halos with  $15 < V_{\max} < 25 \text{ km s}^{-1}$ . There is also a significant fraction of WDM counterpart halos to CDM field halos with  $15 < V_{\max} < 25 \text{ km s}^{-1}$  that have a  $V_{\max}$  below our resolution limit,  $V_{\max} < 8 \text{ km s}^{-1}$  (not shown). We do include these halos in the subsequent analysis.

The median rotation curves of the L7, THM2 and S229 WDM models, shown in the top row panels of Figure 7, fall uniformly below the CDM rotation curves for both  $V_{\max}$  sets. The reduction in the median WDM rotation curves relative to CDM is more pronounced in the lower mass halo sets (top right panel) for the WDM halos with  $V_{\max} > 8 \text{ km s}^{-1}$ . The median rotation curves of the L7, S229, and THM2 WDM models are similar for both  $V_{\max}$  sets, indicating that

each WDM model has, on average, a similar reduction in the central density of their DM halo relative to CDM.

The bottom panels of Figure 7 show the ratio of the WDM field halo density profiles to CDM. The median density ratios of the Local Group WDM field halo counterparts to CDM field halos with  $V_{\max} > 25 \text{ km s}^{-1}$  (bottom left panel) show that the CDM and WDM density profiles converge in the outer halo near  $r = 20 h^{-1} \text{ kpc}$ . The inner region of WDM density profiles reach an average reduction of  $\sim 40\%$  at  $r \leq 1 h^{-1} \text{ kpc}$ . For CDM field halos with  $15 < V_{\max} < 25 \text{ km s}^{-1}$ , the median density ratios of the corresponding Local Group WDM field halo sets (bottom right panel) show the WDM halos with  $V_{\max} > 15 \text{ km s}^{-1}$  are less dense than their CDM counterparts throughout, and are on average  $\sim 60\%$  less dense at  $r = 1 h^{-1} \text{ kpc}$ . Including the WDM field halos with  $V_{\max} > 8 \text{ km s}^{-1}$  in the comparison lowers the median density ratio an additional 10% in the central  $r \leq 1 h^{-1} \text{ kpc}$  and an additional 20% at  $r = 10 h^{-1} \text{ kpc}$  near the average halo virial radius. The median density ratios of the L7, S229, and THM2 WDM models are quantitatively similar at all radii for both  $V_{\max}$  sets and independent of the limiting WDM halo mass.

The reduction in the WDM central density is related to later formation times of WDM halos relative to CDM halos, which collapse earlier when the background matter density of the universe is greater. For both  $V_{\max}$  sets, there is considerable scatter in the individual halo density ratios at all radii. This spread in internal density ratios is reflected in the WDM rotation curves of the both mass set in the top panels. The CDM rotation curves are tightly clustered around the median, while the WDM sets show a larger degree of scatter. We find that, for an individual CDM halo, it is difficult to predict the exact amount of reduction in the corresponding WDM halo density profile (and likewise the rotation curve), however, in general, the less massive the CDM field halo the greater the reduction in the density profile (rotation curve) at all radii.

The internal properties of the WDM subhalos of the Thelma and Louise host halos are also significantly different than their CDM counterparts. We follow the same selection process for the host subhalos sets, with the exception that the CDM subhalos and their WDM counterparts are required to be within the virial radius of either host. For the  $V_{\max} > 25 \text{ km s}^{-1}$  subhalo sets, shown in the left column of Figure 8, the median rotation curves and median density profile ratios of each DM model are quantitatively similar to the median values of the  $V_{\max} > 25 \text{ km s}^{-1}$  Local Group field halos. The L7, S229, and THM2 WDM models each have a  $\sim 40\%$  reduction at  $r \leq 1 h^{-1} \text{ kpc}$  in the median density ratios and a  $\sim 5 \text{ km s}^{-1}$  drop in the median WDM rotation curves relative to the median CDM rotation curve, just as we found for the Local Group field halos. We find no significant difference in the L7, S229, and THM2 model median rotation curves or density profile ratios.

The median rotation curve of CDM subhalos with  $15 \text{ km s}^{-1} < V_{\max} < 25 \text{ km s}^{-1}$  is also similar to the CDM Local Group field halo median rotation curve. The median rotation curves of the WDM subhalo counterparts with  $V_{\max} > 15 \text{ km s}^{-1}$  (shown in the top right panel of Figure 8), however, have only a few  $\text{km s}^{-1}$  reduction in magnitude relative to CDM. The median density ratios of the WDM subhalos with  $V_{\max} > 15 \text{ km s}^{-1}$  show only a 40% reduction

in the central density relative to CDM. This is a smaller decrease than was found for WDM Local Group field halos of the same  $V_{\max}$  cut. There is considerable scatter around the median for the individual density profile ratios of the WDM subhalos with  $V_{\max} > 15 \text{ km s}^{-1}$  that is likely due to tidal stripping effects in both the CDM and WDM subhalos. Including the WDM subhalos with  $V_{\max} > 8 \text{ km s}^{-1}$  brings better agreement with the Local Group field halo results for the same  $V_{\max}$  selection criteria. The median WDM density profiles are then reduced relative to CDM by 60% at all radii out to  $r = 10 h^{-1} \text{ kpc}$ , and the median WDM rotation curves show a more significant decrease on the order of  $\sim 10 \text{ km s}^{-1}$ . For the subhalo sets, we also find no significant difference in the L7, S229, and THM2 model subhalo internal properties. Similar to the Local Group field halo results, we find that, on average, the less massive the CDM subhalo, the greater reduction in the corresponding WDM density profile. Tidal stripping effects, however, can complicate a comparison of a single subhalo between CDM and WDM models.

Figure 9 shows the  $V_{\max}$  relation between the Local Group field halos in WDM and CDM. Halos were selected by choosing Local Group CDM field halos with a  $V_{\max} > 8 \text{ km s}^{-1}$  and then identifying WDM halo counterparts that satisfy the halo correlation criterion described in Section 2. The orange curve shows the one-to-one correspondence between WDM and CDM. All Local Group WDM field halos fall below the orange curve and show a trend of increasingly smaller  $V_{\max}$  relative to the CDM values. The gray dashed curve in Figure 9 shows a fit to the  $V_{\max}$  relation of

$$\frac{V_{\max}(\text{WDM})}{V_{\max}(\text{CDM})} = 1 - \left( \frac{V_{\max}(\text{CDM})}{V_0} \right)^\beta, \quad (4)$$

where  $V_0 = 10.6 \text{ km s}^{-1}$  and  $\beta = -1.58$  for all WDM halos combined. The individual fits to the L7, S229, and THM2 models are not shown, but each is very similar to the combined fit. We note that  $V_{\max}$  values below  $V_{\max} = 15 \text{ km s}^{-1}$  were included in order to obtain a more accurate accounting of the turnover in the  $V_{\max, \text{WDM}} - V_{\max, \text{CDM}}$  relation. The  $V_{\max, \text{WDM}} - V_{\max, \text{CDM}}$  relation summarizes the increased suppression of the WDM halo central density relative to CDM at smaller halo masses.

#### 4 ABUNDANCE OF FIELD HALOS

The Missing Satellites and TBTF problems of CDM in the Local Group persist in the abundance and kinematics of field dwarf galaxies (Zavala et al. 2009; Klypin et al. 2015; Papastergis et al. 2015) motivating the exploration of non-linear evolution of WDM models in cosmological volumes. The redshift zero velocity function of field DM halos in a homogeneously-resolved,  $N_p = 512^3$   $N$ -body simulation of a  $L = 25 h^{-1} \text{ Mpc}$  box for the L7, S229, THM2 and CDM models are shown in Figure 10. The CDM velocity function increases monotonically towards small mass down to  $V_{\max} = 30 \text{ km s}^{-1}$ . We calculate a power law fit to the CDM velocity function that is based on the analytic approximation of Klypin et al. (2015) to the Bolshoi simulation results (Klypin et al. 2011). Our fit is very similar to the Klypin et al. (2015) fit with a power law exponent of  $n = -2.8$  and a  $\sim 20\%$  increase in the normalization. The analytic fit is shown in Figure 10 to be in good agreement with the

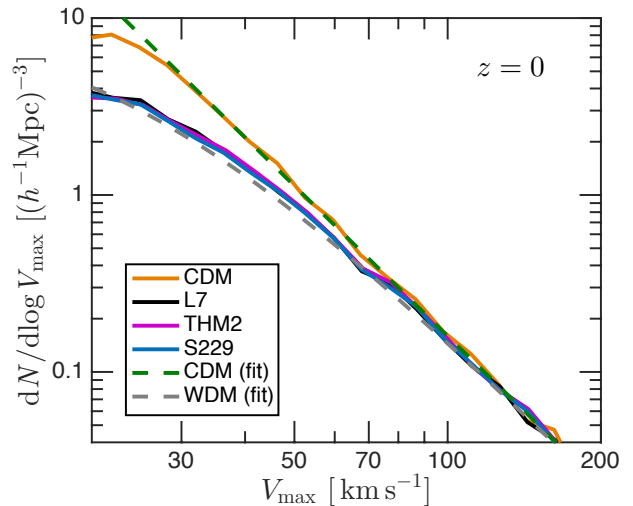


**Figure 10.** The circular velocity functions of field halos in cosmological volume simulations for the CDM (orange), L7 (black), S229 (blue) and THM2 (magenta) DM models at redshift  $z = 0$ . The dashed green and grey curves respectively represent the CDM and thermal  $m = 2 \text{ keV}$  WDM analytic approximations to the velocity functions. Our results show a good agreement with the analytic fits down to  $V = 30 \text{ km s}^{-1}$ . The sterile neutrino and thermal WDM velocity functions are similar for the full range of halo masses and have a maximum suppression of a factor of 2 relative to low-mass CDM halo abundances.

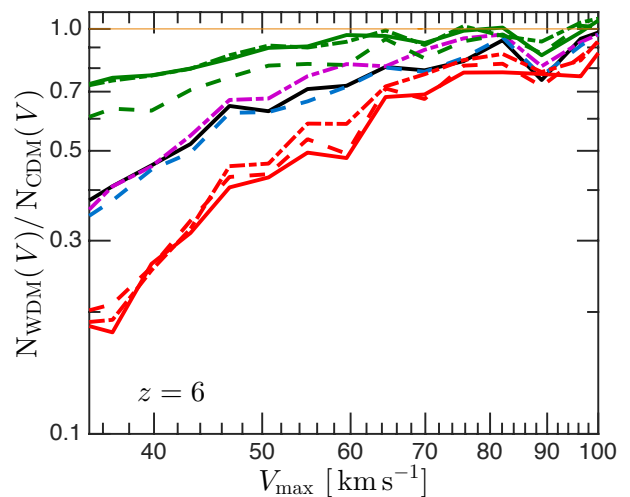


**Figure 11.** The ratio of the circular velocity functions of WDM models to CDM at a redshift of  $z = 6$ . The WDM models shown: L46 (solid; green), S220 (dashed; green), THM2.9 (dash-dot; green), L7 (solid; black), S229 (dashed; blue), THM2 (dash-dot; magenta), L48 (solid; red), S208 (dashed; red), THM1.6 (dash-dot; red). The WDM model velocity function ratios cluster into three groups according to their respective warmth, with only a small  $\sim 5\%$  variation in the velocity function ratios between WDM models of comparable warmth.

simulation results down to  $V_{\max} = 30 \text{ km s}^{-1}$ , below which numerical effects cause the CDM velocity function to turn over.

The L7, S229, and THM2 WDM model velocity functions agree with the CDM velocity function for larger mass halos with  $V_{\max} > 80 \text{ km s}^{-1}$ , but are suppressed relative to CDM for low-mass halos, reaching a factor of two suppression at  $V_{\max} = 30 \text{ km s}^{-1}$ . The sterile neutrino models and thermal WDM velocity functions agree with each other and an analytic fit to a  $m = 2 \text{ keV}$  thermal WDM velocity function, where the equation is taken from Klypin et al. (2015) and modified by our CDM power law exponent and normalization values. The low-mass suppression in the WDM velocity function relative to CDM is related to the reduction in the WDM halo central density profiles found in the previous section and shown in Figure 9. For halos of the mass range considered here, the WDM halos at a fixed abundance are the counterparts to CDM halos of the same abundance, which corresponds to a leftward shift of the CDM velocity function to the WDM velocity function. However, at smaller masses below the resolution of these simulations, the suppression of structure formation in WDM models would become more prevalent, resulting in CDM halos where a WDM counterpart does not form. This would correspond to a decrease in WDM halo abundance relative to CDM at fixed  $V_{\max}$ .

The ratio of the velocity function between WDM and CDM models at redshift  $z = 6$  are shown in Figure 11. We consider a broader range of models here. The velocity function ratios of all the A14 (solid curves) and V15 (dashed curves) sterile neutrino models and their thermal equivalent models (dot-dashed curves) are shown. The relative suppression between WDM and CDM abundances correlates with the warmth of the WDM models, as indicated by the convergence of the curves to three velocity function ratios at  $V_{\max} = 40 \text{ km s}^{-1}$  (with the exception of the S220 model). There are some variations between the velocity functions of the two sterile neutrino models and their thermal best-fit model at intermediate scales between  $45 \text{ km s}^{-1} < V_{\max} < 60 \text{ km s}^{-1}$ . This difference is on the 5% – 10% level, and is likely not differentiable by future high-redshift galaxy surveys. It does suggest, however, that early stages of halo formation may have a relevant differences that could impact the quasi-linear regime, which we explore in the next section.

The agreement of abundances of field halos in the thermal and sterile neutrino WDM models, where suppression of low-mass halo formation is significant relative to CDM, is similar to the abundance results of Local Group halos shown in Figure 5. Differences in the shape of the linear matter power spectrum between thermal and sterile neutrino WDM models are washed out in the deeply nonlinear regime, even at high redshift.

## 5 QUASI-LINEAR REGIME

The progression from the significant differences between thermal WDM and resonantly-produced sterile neutrino WDM models in the linear matter power spectrum, that sets the initial conditions for numerical simulations, to minimal observable differences in the nonlinear measures we have

explored at redshift zero motivates the study of an intermediate, quasi-linear regime. We consider growth of structure in the quasi-linear regime by determining the 3D nonlinear matter power spectrum of the homogeneously-resolved cosmological simulations at  $z \sim 3 - 6$  described in the previous section. Viel et al. (2012) did convergence testing for  $N$ -body simulations with the same cosmology, simulation box size, and number of particles, and found their power spectra converged to  $k = 50 h \text{ Mpc}^{-1}$ . We therefore set  $k = 50 h \text{ Mpc}^{-1}$  as our limiting scale.

Figure 12 shows the ratio of each WDM model’s matter power spectrum to the CDM matter power spectrum at redshift  $z = 2.98$  (solid) and  $z = 5.429$  (dashed) in the left-hand column. Each row in Figure 12 gives the results for a set of WDM models of comparable warmth that includes two sterile neutrino models (one for each V15 and A14) and their thermal equivalent WDM model. The thin, solid curves in each panel of the left hand column show the linear matter power spectrum ratios for each WDM model relative to CDM. By redshift  $z = 5.429$ , the nonlinear matter power spectrum calculated from the simulations have diverged from the linear matter power spectrum by at least a few percent at  $k = 5 h \text{ Mpc}^{-1}$  for all but the coldest WDM models (top left panel), and all WDM models show significant evolution from the linear matter power spectrum on scales of  $k = 10 h \text{ Mpc}^{-1}$ . Viel et al. (2013) find that a few percent suppression in the  $m = 2 \text{ keV}$  thermal WDM 3D nonlinear matter power spectrum relative to CDM at  $k = 10 h \text{ Mpc}^{-1}$  is differentiable in the Lyman- $\alpha$  forest 1D flux power spectrum at these redshifts. The scales and the degree of power spectrum suppression of the sterile neutrino models relative to CDM that we find here is, therefore, relevant for Lyman- $\alpha$  forest measurements (Viel et al. 2012, 2013).

The right-hand column of Figure 12 shows the power spectrum ratios of the sterile neutrino models with respect to the matter power spectrum of the equivalent thermal WDM model for  $z = 2.98$  (solid) and  $z = 5.429$  (dashed). The S229 and S208 model power spectrum ratios show similar departures from thermal WDM for  $k > 2 h \text{ Mpc}^{-1}$  at both  $z = 2.98$  and  $z = 5.429$ . Compared to these two warmer V15 models, the S220 model (top right panel) has a slightly greater reduction in power spectrum relative to thermal WDM at  $k = 50 h \text{ Mpc}^{-1}$ . The A14 models show a greater variation in the power spectrum ratios with their thermal equivalent models than the qualitatively uniform V15 models. The coldest A14 model, L46, is consistent with its thermal equivalent on all scales and redshifts. The L7 model (middle right panel) shows suppression relative to the power spectrum of the  $m = 2 \text{ keV}$  thermal WDM model for scales  $k > 1 h \text{ Mpc}^{-1}$ . The warmest A14 model, L8 (shown in the bottom right panel), has more power relative to thermal WDM for  $1 < k < 5(10) h \text{ Mpc}^{-1}$  at  $z = 5.429(2.98)$ , and increasingly less power than thermal WDM on smaller scales.

The relative strength of the resonant sterile neutrino matter power spectrum at a fixed scale compared to a thermal equivalent WDM model does not correlate with warmth or the details of the resonant sterile neutrino production calculation, i.e. V15 and A14 models. For example, the L7 model shows enhanced suppression relative to the S229 model, but the L8 model has more power than the S208

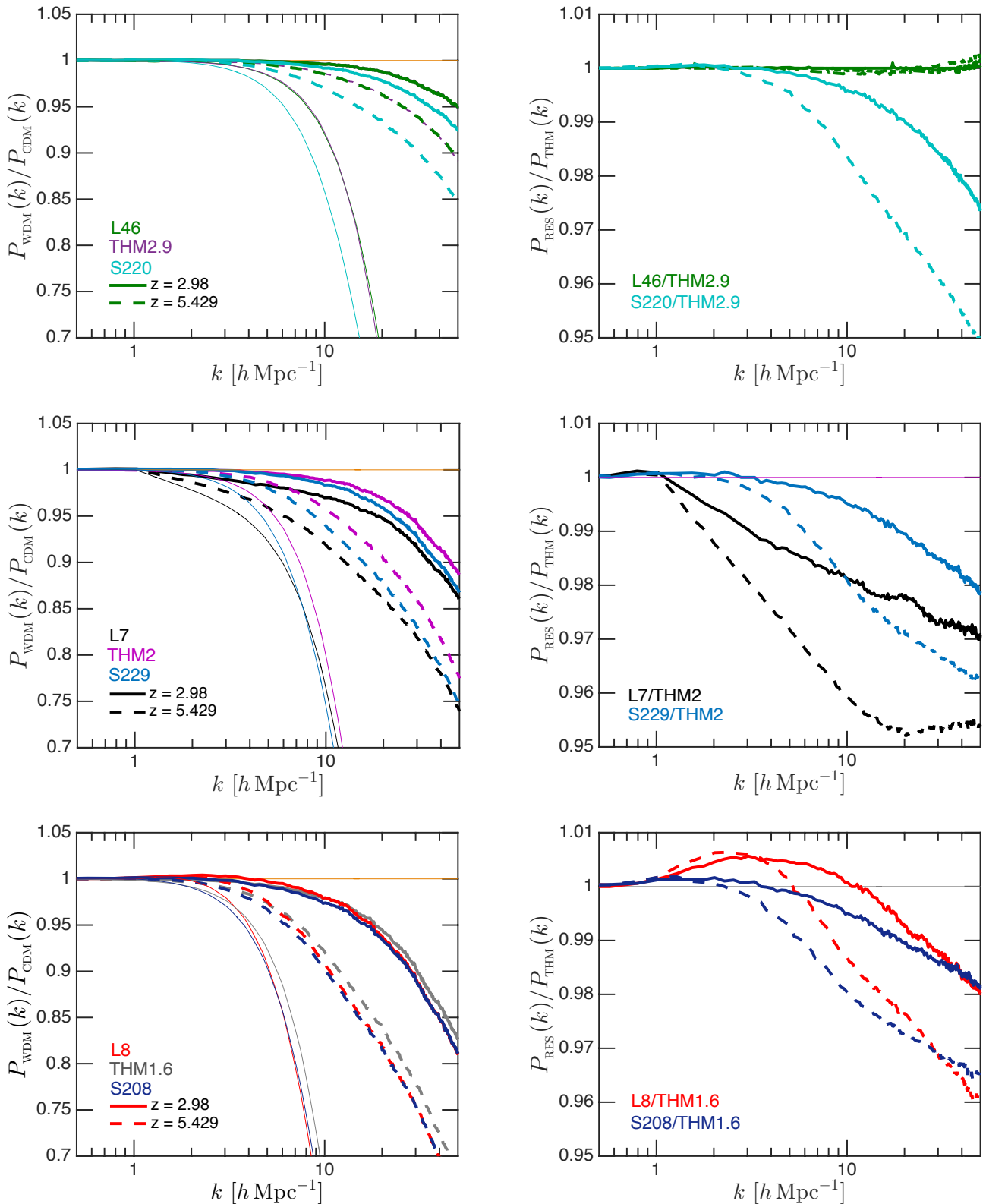


**Figure 12.** *Left column:* ratio of the 3D matter power spectrum for WDM models with respect to CDM for redshifts  $z = 2.98$  (solid) and  $z = 5.429$  (dashed). *Right column:* ratio of the 3D matter power spectrum of sterile neutrino models with respect to a thermal equivalent WDM model. Rows divide WDM models into groups of similar model warmth. *Top Row:* L46 (green), S220 (cyan), THM2.9 (purple). *Middle Row:* L7 (black), S229 (blue), and THM2 (magenta). *Bottom Row:* L8 (red), S208 (blue), THM1.6 (grey). Solid, thin curves (left column) are the linear matter power spectrum ratios of WDM to CDM. The 3D matter power spectrum of the sterile neutrino and thermal WDM models suppress small-scale power relative to CDM, but to differing degrees depending on the warmth of the model. The matter power spectrum ratios on scales above  $k > 1 h \text{ Mpc}^{-1}$  show differences at the few percent level, which is significant, between the sterile neutrino and thermal WDM models.

model for  $k < 50 h \text{Mpc}^{-1}$ . The detailed shape of transfer function is, therefore, the most relevant parameter for determining the relative power in the quasi-linear regime for the scales probed here.

A direct comparison with measurements of the Lyman- $\alpha$  forest is beyond the scope of this paper. However, if a few percent difference in the 3D nonlinear matter power for  $k = 10 h \text{Mpc}^{-1}$  at  $z = 3 - 5$  can distinguish thermal WDM from CDM, as claimed (Viel et al. 2012, 2013), then the percent level differences of sterile neutrino models from thermal WDM that we find here are significant. A full Lyman- $\alpha$  study should then be able to differentiate between sterile neutrino models and a thermal equivalent model, where linear matter power spectrums differ at a few percent level on scales above the half-mode suppression scale. Constraints on WDM particle masses for models with non-thermal distributions, such as sterile neutrinos, from thermal WDM tests are therefore inadequate. Future Lyman- $\alpha$  observations that can probe scales of  $10 < k < 50 h \text{Mpc}^{-1}$  would have great ability to test these models further.

## 6 DISCUSSION AND CONCLUSIONS

In this paper, we have presented a variety of simulations – both zoom-ins of Local Group analogs and homogeneously-resolved cosmological volumes – of sterile neutrino dark matter. The focus of our work is on resonantly-produced sterile neutrinos, which result in transfer functions that differ significantly from the standard assumption of a thermal relic. We use transfer functions from both A14 and V15, the latter being a more accurate calculation of the former, and best-fit thermal WDM approximations. This allows a detailed exploration of transfer function shape on Local Group halo properties while evaluating the resonant sterile neutrino models that are best able to explain the 3.55 keV anomalous X-ray signal found by various surveys (Bulbul et al. 2014; Boyarsky et al. 2014).

We find the density profiles, shapes, and mass assembly histories of the Local Group host halo pairs are similar for all DM models, irrespective of the warmth of the WDM model. The abundance of low-mass subhalos in each WDM host is reduced significantly relative to CDM and depends on the warmth of the model. The reduction in the number of low-mass subhalos alleviates the Missing Satellites problem. However, the number of Local Group subhalos could also be used to rule out these and similar sterile neutrino models if the number of MW and M31 satellite galaxies exceeds the predicted number of WDM halos. This depends on the total number of dwarf galaxies found by future surveys (Tollerud et al. 2008; Hargis et al. 2014) and the minimum DM halo mass that would host a detectable satellite galaxy (Koposov et al. 2008; Polisensky & Ricotti 2011; Kennedy et al. 2014; Horiuchi et al. 2014). The abundance of subhalos at the resolution limit of the warmest sterile neutrino model considered here, L8, is near the current satellite count for both the MW and M31 and could be ruled out in the near future by DES, LSST or WFIRST (Ivezic et al. 2008; Bechtol et al. 2015; Spergel et al. 2015). The abundance of low-mass field halos is also suppressed relative to CDM, with a suppression that is well-described by the thermal-equivalent mass of the WDM model.

The internal properties of WDM Local Group field halos and MW/M31 subhalos also show differences relative to their CDM counterparts: the WDM halos have a reduced central density that becomes more pronounced for lower halo masses. However, even WDM halos several times more massive than the WDM model half-mode mass, below which free-streaming effects are typically considered most relevant, show a 40% decrease, on average, in their central density halos relative to CDM. A similar result was found for subhalos in thermal WDM simulations of MW-sized DM hosts (Polisensky & Ricotti 2014; Schneider et al. 2014) and field halos in simulations using thermal approximations to resonant sterile neutrino WDM models (Bose et al. 2015). This is unsurprising, as we find the median density profile ratios and rotation curves do not show any significant variation between thermal and resonant sterile neutrino WDM models.

Importantly, we find that the half-mode mass is largely predictive of the number of Local Group halos, the abundance of low-mass halos in the field, and for the density reduction in WDM halos relative to CDM. For the range of scales probed here, nonlinear evolution washes away linear matter power spectrum differences other than overall suppression of small-scale power that is effectively captured by a single parameter, the half-mode mass. However, the more accurate resonant sterile neutrino transfer function should be used when testing sterile neutrino models with observed satellite galaxy counts, as differences at the 10% level may persist and are important in constraining dark matter models via the luminosity function of Local Group satellites (Horiuchi et al. 2015).

At high redshift, in the quasi-linear regime on scales that are relevant for Lyman- $\alpha$  forest measurements, we find quantitative differences in the 3D matter power spectrum of resonantly-produced sterile neutrino and thermal WDM models. The differences in the linear matter power spectrum between the resonant sterile neutrino DM models (based on two separate calculations by V15 and A14) and their thermal equivalent WDM model are preserved in the redshift  $z = 3 - 5$  matter power spectrum of these models at a few percent level on small scales. The 3D matter power spectrum differences found here could translate into relevant differences in the Lyman- $\alpha$  forest 1D flux power spectrum (Viel et al. 2013). Measurements in the Lyman- $\alpha$  forest may be able to discern between structure formation resulting from different sterile neutrino DM models and thermal WDM models before the epoch where nonlinear evolution washes away differences in the linear matter power spectrum.

We find that the exact transfer function shape is important for placing constraints on resonantly-produced sterile neutrino WDM models. Thermal WDM approximations are sufficient for some studies, such as the internal properties of Local Group halos, and abundance of halos in the Local Group or large cosmological volumes. However, careful consideration should be given to constraints when comparing Local Group luminosity functions to subhalo mass functions (Horiuchi et al. 2015) and when comparing 3D matter power spectrum results from cosmological volume simulations to Lyman- $\alpha$  forest measurements. Constraints on resonantly-produced sterile neutrino DM models derived from thermal WDM studies could prove out, however, simple extrapolations of those results to

resonantly-produced sterile neutrino WDM models have been shown here to be incorrect. Future surveys of the Local Group by LSST, DES, and WFIRST, as well as detailed studies of the Lyman- $\alpha$  forest that consider scales in the quasi-linear regime, have great power to test resonant sterile neutrino models.

## 7 ACKNOWLEDGMENTS

We thank Tejaswi Venumadhav and Francis-Yan Cyr-Racine for useful discussions. The authors acknowledge the University of Maryland supercomputing resources (<http://www.it.umd.edu/hpcc>) made available for conducting the research reported in this paper. MB-K acknowledges support from NASA through Hubble Space Telescope theory grants (programs AR-12836 and AR-13888) from the Space Telescope Science Institute (STScI), which is operated by the Association of Universities for Research in Astronomy (AURA), Inc., under NASA contract NAS5-26555. Support for S.G.K. was provided by NASA through Einstein Postdoctoral Fellowship grant number PF5-160136 awarded by the Chandra X-ray Center, which is operated by the Smithsonian Astrophysical Observatory for NASA under contract NAS8-03060. K.N.A. is partially supported by NSF CAREER Grant No. PHY-11-59224 and NSF Grant No. PHY-1316792.

## REFERENCES

- Abazajian K., 2006, *Phys. Rev. D*, **73**, 063506
- Abazajian K. N., 2014, *Physical Review Letters*, **112**, 161303
- Abazajian K. N., Fuller G. M., 2002, *Phys. Rev. D*, **66**, 023526
- Anderhalden D., Diemand J., Bertone G., Macciò A. V., Schneider A., 2012, *J. Cosmology Astropart. Phys.*, **10**, 47
- Anderhalden D., Schneider A., Macciò A. V., Diemand J., Bertone G., 2013, *J. Cosmology Astropart. Phys.*, **3**, 14
- Asaka T., Blanchet S., Shaposhnikov M., 2005, *Physics Letters B*, **631**, 151
- Avila-Reese V., Colín P., Valenzuela O., D’Onghia E., Firmani C., 2001, *ApJ*, **559**, 516
- Baur J., Palanque-DeLabrouille N., Yèche C., Magneville C., Viel M., 2015, preprint, ([arXiv:1512.01981](https://arxiv.org/abs/1512.01981))
- Bechtol K., et al., 2015, *ApJ*, **807**, 50
- Bode P., Ostriker J. P., Turok N., 2001, *ApJ*, **556**, 93
- Bose S., Hellwing W. A., Frenk C. S., Jenkins A., Lovell M. R., Helly J. C., Li B., 2015, preprint, ([arXiv:1507.01998](https://arxiv.org/abs/1507.01998))
- Boyarisky A., Ruchayskiy O., Iakubovskiy D., Franse J., 2014, *Physical Review Letters*, **113**, 251301
- Boyarisky A., Franse J., Iakubovskiy D., Ruchayskiy O., 2015, *Physical Review Letters*, **115**, 161301
- Boylan-Kolchin M., Bullock J. S., Kaplinghat M., 2011, *MNRAS*, **415**, L40
- Boylan-Kolchin M., Bullock J. S., Kaplinghat M., 2012, *MNRAS*, **422**, 1203
- Brook C. B., et al., 2011, *MNRAS*, **415**, 1051
- Bulbul E., Markevitch M., Foster A., Smith R. K., Loewenstein M., Randall S. W., 2014, *ApJ*, **789**, 13
- Bullock J. S., Kravtsov A. V., Weinberg D. H., 2000, *ApJ*, **539**, 517
- Colombi S., Dodelson S., Widrow L. M., 1996, *ApJ*, **458**, 1
- Di Cintio A., Brook C. B., Macciò A. V., Stinson G. S., Knebe A., Dutton A. A., Wadsley J., 2014, *MNRAS*, **437**, 415
- Dodelson S., Widrow L. M., 1994, *Physical Review Letters*, **72**, 17
- Dunstan R. M., Abazajian K. N., Polisensky E., Ricotti M., 2011, preprint, ([arXiv:1109.6291](https://arxiv.org/abs/1109.6291))
- Flores R. A., Primack J. R., 1994, *ApJ*, **427**, L1
- Frenk C. S., White S. D. M., 2012, *Annalen der Physik*, **524**, 507
- Garrison-Kimmel S., Rocha M., Boylan-Kolchin M., Bullock J. S., Lally J., 2013, *MNRAS*, **433**, 3539
- Garrison-Kimmel S., Boylan-Kolchin M., Bullock J. S., Lee K., 2014a, *MNRAS*, **438**, 2578
- Garrison-Kimmel S., Boylan-Kolchin M., Bullock J. S., Kirby E. N., 2014b, *MNRAS*, **444**, 222
- Governato F., et al., 2010, *Nature*, **463**, 203
- Governato F., et al., 2012, *MNRAS*, **422**, 1231
- Hahn O., Abel T., 2011, *MNRAS*, **415**, 2101
- Hargis J. R., Willman B., Peter A. H. G., 2014, *ApJ*, **795**, L13
- Horiuchi S., Humphrey P. J., Oñorbe J., Abazajian K. N., Kaplinghat M., Garrison-Kimmel S., 2014, *Phys. Rev. D*, **89**, 025017
- Horiuchi S., Bozek B., Abazajian K. N., Boylan-Kolchin M., Bullock J. S., Garrison-Kimmel S., Oñorbe J., 2015, *MNRAS* (accepted)
- Iakubovskiy D., Bulbul E., Foster A. R., Savchenko D., Sadova V., 2015, preprint, ([arXiv:1508.05186](https://arxiv.org/abs/1508.05186))
- Ivezic Z., et al., 2008, preprint, ([arXiv:0805.2366](https://arxiv.org/abs/0805.2366))
- Kennedy R., Frenk C., Cole S., Benson A., 2014, *MNRAS*, **442**, 2487
- Kirby E. N., Bullock J. S., Boylan-Kolchin M., Kaplinghat M., Cohen J. G., 2014, *MNRAS*, **439**, 1015
- Klypin A., Kravtsov A. V., Valenzuela O., Prada F., 1999, *ApJ*, **522**, 82
- Klypin A. A., Trujillo-Gomez S., Primack J., 2011, *ApJ*, **740**, 102
- Klypin A., Karachentsev I., Makarov D., Nasonova O., 2015, *MNRAS*, **454**, 1798
- Knollmann S. R., Knebe A., 2009, *ApJS*, **182**, 608
- Koposov S., et al., 2008, *ApJ*, **686**, 279
- Kravtsov A. V., Gnedin O. Y., Klypin A. A., 2004, *ApJ*, **609**, 482
- Larson D., et al., 2011, *ApJS*, **192**, 16
- Lovell M. R., et al., 2012, *MNRAS*, **420**, 2318
- Lovell M. R., Frenk C. S., Eke V. R., Jenkins A., Gao L., Theuns T., 2014, *MNRAS*, **439**, 300
- McConnachie A. W., 2012, *AJ*, **144**, 4
- Moore B., 1994, *Nature*, **370**, 629
- Moore B., Ghigna S., Governato F., Lake G., Quinn T., Stadel J., Tozzi P., 1999, *ApJ*, **524**, L19
- Oñorbe J., Boylan-Kolchin M., Bullock J. S., Hopkins P. F., Kereš D., Faucher-Giguère C.-A., Quataert E., Murray N., 2015, *MNRAS*, **454**, 2092
- Obreschkow D., Power C., Bruderer M., Bonvin C., 2013, *ApJ*, **762**, 115
- Papastergis E., Giovanelli R., Haynes M. P., Shankar F., 2015, *A&A*, **574**, A113
- Patwardhan A. V., Fuller G. M., Kishimoto C. T., Kusenko A., 2015, *Phys. Rev. D*, **92**, 103509
- Peñarrubia J., Pontzen A., Walker M. G., Koposov S. E., 2012, *ApJ*, **759**, L42
- Polisensky E., Ricotti M., 2011, *Phys. Rev. D*, **83**, 043506
- Polisensky E., Ricotti M., 2014, *MNRAS*, **437**, 2922
- Power C., Navarro J. F., Jenkins A., Frenk C. S., White S. D. M., Springel V., Stadel J., Quinn T., 2003, *MNRAS*, **338**, 14
- Primack J. R., 2015, preprint, ([arXiv:1505.02821](https://arxiv.org/abs/1505.02821))
- Schneider A., Smith R. E., Macciò A. V., Moore B., 2012, *MNRAS*, **424**, 684
- Schneider A., Anderhalden D., Macciò A. V., Diemand J., 2014, *MNRAS*, **441**, L6
- Shi X., Fuller G. M., 1999, *Physical Review Letters*, **82**, 2832

- Spergel D., et al., 2015, preprint, ([arXiv:1503.03757](#))
- Springel V., 2005, *MNRAS*, **364**, 1105
- Tollerud E. J., Bullock J. S., Strigari L. E., Willman B., 2008, *ApJ*, **688**, 277
- Venumadhav T., Cyr-Racine F.-Y., Abazajian K. N., Hirata C. M., 2015, preprint, ([arXiv:1507.06655](#))
- Viel M., Lesgourgues J., Haehnelt M. G., Matarrese S., Riotto A., 2005, *Phys. Rev. D*, **71**, 063534
- Viel M., Markovič K., Baldi M., Weller J., 2012, *MNRAS*, **421**, 50
- Viel M., Becker G. D., Bolton J. S., Haehnelt M. G., 2013, *Phys. Rev. D*, **88**, 043502
- Wang J., White S. D. M., 2007, *MNRAS*, **380**, 93
- Zavala J., Jing Y. P., Faltenbacher A., Yepes G., Hoffman Y., Gottlöber S., Catinella B., 2009, *ApJ*, **700**, 1779
- Zolotov A., et al., 2012, *ApJ*, **761**, 71
- de Gouvêa A., 2005, *Phys. Rev. D*, **72**, 033005